



Measurements by x-ray diffraction of the temperature dependence of lattice parameter and crystallite size for isostatically-pressed graphite

Keith R. Hallam^{a,*}, James Edward Darnbrough^b, Charilaos Paraskevoulakos^a,
Peter J. Heard^a, T. James Marrow^b, Peter E.J. Flewitt^{a,c}

^a Interface Analysis Centre, School of Physics, HH Wills Physics Laboratory, Tyndall Avenue, Bristol, BS8 4TS, United Kingdom

^b Department of Materials, University of Oxford, Parks Road, Oxford, OX1 3PH, United Kingdom

^c School of Physics, HH Wills Physics Laboratory, Tyndall Avenue, Bristol, BS8 4TS, United Kingdom

ARTICLE INFO

Article history:
Received 24 March 2021
Revised 4 June 2021
Accepted 6 June 2021

Keywords:
Polygranular graphite
X-ray diffraction
Temperature
Lattice parameter
Crystallite size
Microstrain

ABSTRACT

Synthetic polygranular graphites of various grades and manufacturing routes are used in nuclear reactors for power generation, and may be used in potential fourth generation and other advanced reactor designs that will operate at higher temperature. Attention is given in this paper to isostatically-moulded synthetic polygranular graphites with porosities in the range 8% to 18%. The lattice parameters a and c for the hexagonal graphite have been measured over the temperature range from room temperature to 800°C by x-ray diffraction. The variation with temperature of the crystal lattice parameters, coherence length (crystallite size) and microstrain are discussed with reference to the microstructure and the relative strength of the bonds in-plane and normal to the graphene layers.

© 2021 The Author(s). Published by Elsevier Ltd.

This is an open access article under the CC BY license (<http://creativecommons.org/licenses/by/4.0/>)

1. Introduction

Nuclear graphites are manufactured in specific grades for use as moderator or reflector material in reactors. Graphite is used because of its low neutron absorption cross-section and high scattering cross-section compared to other materials [1,2]. Currently, in the UK there are a significant number of operating advanced gas-cooled reactors that use Gilsocarbon graphite to moderate the fast neutrons and fulfil structural requirements within the cores. Internationally, there are various potential fourth generation (Gen IV) systems being considered for future power generation, of which some are graphite-moderated. These include the high-temperature, helium-cooled reactor, capable of producing gas output temperatures of about 1000°C, and the molten salt reactor, with its high thermodynamic efficiency. These new, more extreme, nuclear environments illustrate why there is still an interest in interrogating graphites with improved physical and mechanical properties [3]. In this paper, we focus on a polygranular, isostatically-moulded graphite. One key characteristic of isostatically-moulded graphite is that the properties are practically uniform in all macroscopic directions, including the low thermal expansion coefficient. The role of the coefficient of thermal expansion, which varies in particu-

lar crystallographic directions, is very important, through its effect on the internal stresses generated within graphite components by dimensional change from temperature and neutron flux gradients [4,5]. The thermal expansion of graphite, according to Riley's theory [6], is related to changes in lattice vibrations both parallel and perpendicular to the basal plane of the hexagonal graphite structure, and other properties varying with temperature [5,7,8].

To interpret the physical responses of these synthetic graphites, it is important to understand their complex microstructures over the nano to micro length-scales. In general, there are two basic approaches that can be adopted to measure crystallite sizes in materials: (i) direct imaging using, for example, high-resolution transmission electron microscopy (TEM) [9]; and (ii) indirect measurements, including x-ray diffraction (XRD) and Raman spectroscopy [9]. Direct imaging is capable of providing the distribution of crystallite sizes but requires time-consuming specimen preparation and image analysis, and can be limited to relatively small regions of individual specimens. In comparison, XRD averages over a much larger volume of the material. In XRD, crystallite size measurement is ultimately derived from unit cell columns aligned perpendicular to a given set of diffracting planes that are assumed to extend from one edge of the crystallite to the other. Therefore, it is the distribution of unit cell columns, referred to as the coherence length or coherence domain, that is equated to crystallite size. This information is calculated from the width of peaks that arise by diffraction from

* Corresponding author.

E-mail address: k.r.hallam@bristol.ac.uk (K.R. Hallam).

the coherent domains (crystallites) and may be evaluated using either the Scherrer [10,11] or Williamson-Hall [12] methods. The former provides a measure of both the L_a and L_c (length of coherent diffracting domain in the a and c direction, respectively) values while the latter gives a mean measurement of the coherence length (crystallite size). The Williamson-Hall method also yields a measure of the microstrain (i.e. lattice elastic strain).

Interpretation of the XRD traces derived from various natural and synthetic polygranular graphites is complex as it reveals a series of overlapping peaks that affect crystallite size evaluation. In particular, a series of overlapping peaks has been observed in the 2θ range equivalent to the d -spacing 0.22nm to 0.19nm for hexagonal graphite. Various workers have sought to resolve the complexity of peak overlap and peak distortion, invoking a number of interpretations [5,13]. For example, both Babu and Seeha [13] and Li et al [14] have linked the overlap peak geometry in this angular range to the graphite structure. Comparisons of a series of next generation graphites led to the conclusion that all were composed of a turbostratic structure arising from random rotations of crystallites normal to the basal plane of the hexagonal graphite crystal structure [15]. One interpretation is that the graphite structure is a variant of hexagonal graphite, and both this and turbostratic carbon are stacked as graphene layers with a regular spacing but different stacking ordering degree. Hexagonal graphite is an ordered AB stacking structure, but for turbostratic carbon the graphene layers may randomly translate relative to each other and rotate about the normal of these layers. Small local elastic strains arising from crystal defects could potentially induce a change from a hexagonal to a rhombohedral structure (ABC sequence) at the nano length-scale. More recently, on the basis of high-resolution TEM studies März et al [16] proposed that isostatically-moulded graphites have a characteristic 'crazy paving' crystallite structure. This has similarities to a turbostratic structure since, in such a case, the graphite crystallites are oriented parallel but are rotated randomly about the basal plane normal [1]. There is no definitive interpretation to this long-standing problem of evaluating the nano length-scale microstructure of polygranular graphites. For this reason, the analysis outlined in this paper provides information by dissecting the data into the diffracted intensity from well-defined mechanisms and more-complex sources. This allows for known characterisation and exotic defects and microstructures to be deconvoluted, rather than using a less-flexible approach, such as Rietveld [17].

This paper focuses on the temperature dependence of the isostatically-moulded graphite and compares the evaluation of crystallite size and microstrain as functions of temperature, using both the Scherrer and the Williamson-Hall methods. The results are considered with respect to the overall microstructure at the micro and nano length-scales.

2. Material and methods

2.1. Material

The experimental graphite was supplied by Sinosteel Advanced Materials (China). This range of Sinosteel nuclear graphite (SNG) materials was prepared from petroleum coke and coal tar pitch, used as base materials for the filler and binder. Full details of the manufacturing parameters adopted are not disclosed, but the average diameter of the filler particles for the various billets from which test specimens were selected was 20 μ m. These particles were mixed with the pitch binder prior to isostatic pressing in a mould. The as-moulded green billets were then impregnated with pitch and subsequently subjected to a graphitising heat treatment cycle. The final billets from which the samples were selected had nominal properties, as shown in Table 1. The samples were then machined to produce disc specimens 17mm in diameter and ap-

proximately 0.8mm to 0.9mm thick, which were then analysed in their as-prepared state. For each material, individual specimens were prepared in both axial (ax) and transverse (tr) directions with respect to the orientation of the original billets.

2.2. X-ray diffraction

2.2.1. Experimental

A Philips X'Pert Pro diffractometer with a $\text{CuK}\alpha$ radiation source ($\lambda=0.15406\text{nm}$) was used for XRD analysis (40keV generator voltage; 30mA tube emission current). When more complete XRD spectra were acquired, these were between 2θ of 20° to 90° , with a step size of 0.02° and a 1.5s dwell time. Phase and peak identification were then performed using International Centre for Diffraction Data and Crystallography Open Database spectral libraries.

An Anton Parr HTK 1200 high-temperature oven camera was used for studies at elevated temperatures under vacuum, with the SNG graphite specimens fitted to alumina holders. During the work reported here, measurements were taken under vacuum ($\sim 10^{-4}\text{Pa}$) for each specimen at ambient temperature (between 20°C and 24°C ; indicated in some figures here by 'RT'), 200°C , 400°C , 600°C , 800°C and back at ambient ('RT2'). Sample heights were adjusted using the half-cut method following each change in temperature.

To establish calibration for the high-temperature XRD system in terms of both peak position and instrument broadening, a reference lanthanum hexaboride (NIST SRM 660c) powder was used. Individual peak centres and full width half maxima (FWHM) were identified using PANalytical Data Viewer software (Version 1.5a (1.5.1.135)). Although a small systematic trend of increasing FWHM with diffraction angle is expected theoretically, in the present case this was subsumed in the scatter so that a measured mean value of 0.123° was adopted. The true measured peak width for the present Sinosteel graphite specimens was derived from the measured peak minus instrument broadening subtracted in quadrature [18].

2.2.2. Analysis methods

Various workers [10,19] have proposed that broadening of XRD peaks can be produced by a combination of coherence length (one-dimensional crystallite size) and lattice strain. As a consequence, methods have been developed to evaluate these parameters based upon analysis of XRD peak profiles. The process of developing and conducting analysis of the XRD data was undertaken using bespoke scripts within the Matlab environment. Changes observed in the XRD data obtained at different temperatures were considered separately for each Bragg peak. The analyses were divided into two separate steps: (i) the well-established Scherrer approach [10], to evaluate L_a and L_c ; and (ii) the more-refined approach proposed by Williamson and Hall [12], which enables separation of the coherence length (crystallite size) and microstrain.

2.2.2.1. Scherrer analysis. When adopting the Scherrer approach, analysis is based upon the interference produced when x-rays diffract from a material arising from the requirement that there is coherence at a defined length-scale. This scale defines a volume of material, albeit small (nanometre length-scale), where scattering of electromagnetic radiation produces interference. For x-rays, since the diffraction arises from relatively large incident beams, many coherence volumes are sampled and observed. Based upon the work of Warren [20], the size of the two-dimensional layers in graphite can be derived from the breadth of (100)-type diffraction peaks using the Scherrer equation [18], with an appropriate shape factor, k' , so that:

$$L = \frac{k'\lambda}{\beta \cos \theta} \quad (1)$$

Table 1
Material property guideline (provided by Sinosteel Advanced Materials, except where noted).

Material	Density/g.cm ⁻³	Young's modulus/GPa	Compressive strength/MPa	Coefficient of thermal expansion (20°C-600°C)/x10 ⁻⁶ °C	Porosity (open and closed)/%	Porosity (this work) (open and closed)/%
SNG342	1.78	9	65	3.9	18	---
SNG623	1.81	11	93	4.6	17	XRT 9.3 FIB 7.3
						Sum 16.6
SNG722	1.85	12	105	5.1	8	XRT 7.4 FIB 3.3
						Sum 10.7
SNG742	1.83	11	77	4.8	12	---
SNG3420	1.78	9	70	4.0	17	---
SNG7420	1.85	12	84	4.9	15	---

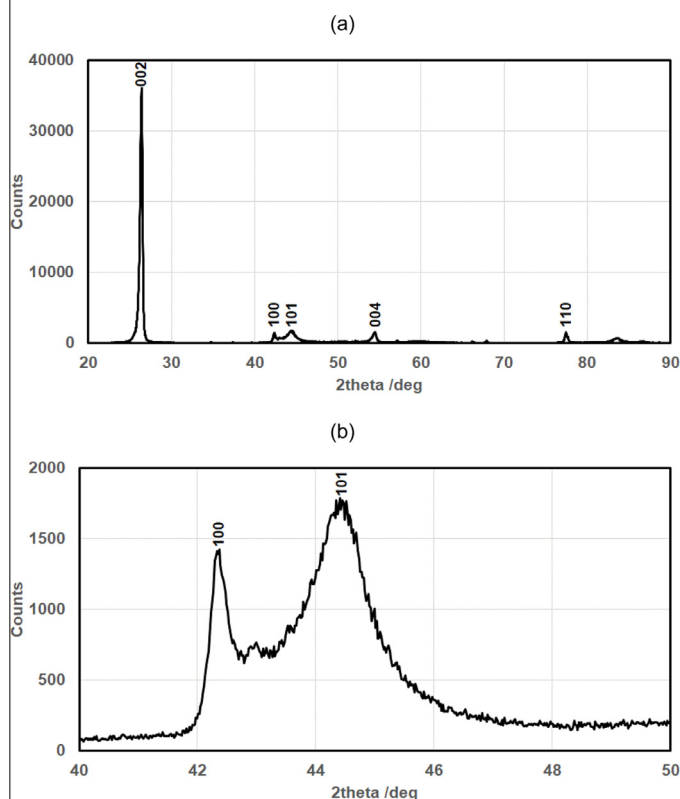


Fig. 1. a) Typical XRD scan of graphite SNG342ax; b) Detail of (100) and (101) diffraction peaks in the 2θ range 40° to 50°.

where λ is wavelength of the incident x-ray beam, β is the peak width at the half maximum intensity and θ is the Bragg diffraction angle. A typical value for k' of 1.84 is adopted [18].

2.2.2.2. Williamson-Hall analysis. Prior to invoking the Williamson-Hall approach, the respective XRD traces were subject to further interrogation and evaluation. The dominant Bragg diffraction peaks used for comparison were (002), (100), (101), (004) and (110) (Fig. 1). To isolate each peak, windows were selected covering the following 2θ ranges: 20° to 30°; 40° to 43.2°; 43.2° to 48°; 52° to 56°; and 76° to 78°. We have adopted a procedure where the peaks, P_{measured} , were then considered separately for asymmetry, by selecting the maximum intensity within the window and declaring this to be the centre¹. Each side was mirrored and the

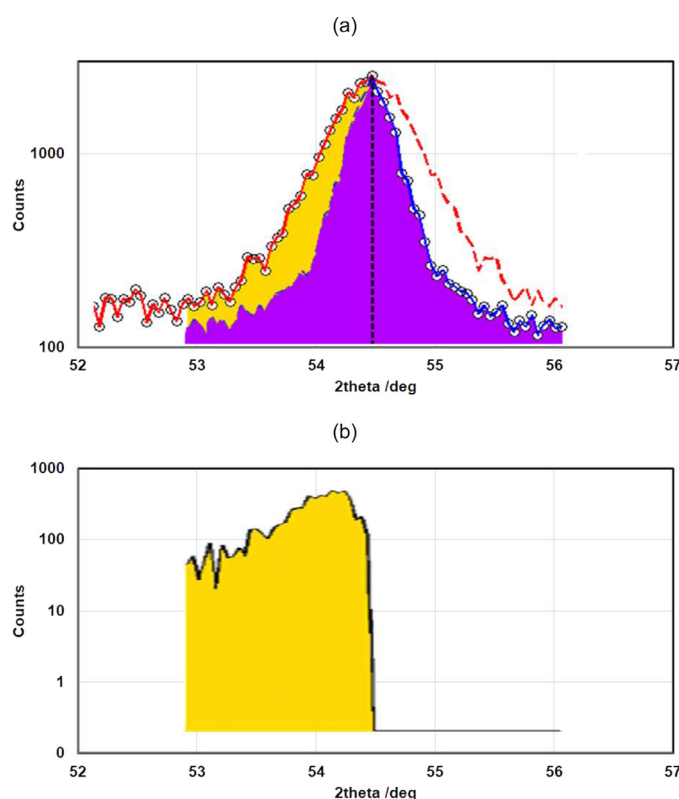


Fig. 2. Peak mirroring to isolate asymmetry: a) Data - black circles; Low 2θ - red; High 2θ - blue; Symmetric peak - purple; Asymmetry - yellow; b) Asymmetry alone.

smaller peak (by sum weighting intensity) was selected as the true symmetrical peak, P_{sym} (purple in Fig. 2a). The difference between the measured and symmetrical peaks was recorded as the total intensity asymmetry of the peak, A_{sym} (yellow in Fig. 2b). This provides a rigorous interrogation of each peak. The symmetrical peak was fitted using a recursive residual minimisation routine created by members of the Institut Laue-Langevin [21].

A nominal starting background was selected as 1 count. All these variables were allowed to be modified by the process to produce the best fit, as declared by minimisation of the residuals between the fit and the data, for the symmetrical peak. The fit can be used to evaluate the shape of the peaks (Lorentzian, Gaussian or a mix), illustrating the coherence of the Bragg diffraction leading to the expected Lorentzian peak shape due to the dominance of wavelength dispersion at high angles. The ratio of asymmetry (A_{sym} /Area under the fitted peak, with the total asymmetry) illustrated in Fig. 2(b) shows the amount and direction of preferen-

¹ Intensity was defined as the maximum intensity within the window; Centre was the position of the maximum intensity; η , the ratio of Lorentzian to Gaussian, was set at 1; Breadth (β), was set at 1°.

tial broadening. Broadening on the high- 2θ side of a peak indicates inhomogeneous compressive strain, and on the low side tensile strain. Interpretation of the source of this asymmetric intensity will be discussed later. This procedure of peak fitting provides an accurate measure of the peak position that can be used to calculate the interplanar distance (d) and, from that, the lattice parameters.

The total broadening of a diffraction peak (β_{total}) is related to the crystallite size (β_{size}) and the microstrain (β_{strain}), as follows:

$$\beta_{\text{total}} = \beta_{\text{size}} + \beta_{\text{strain}} = \frac{0.9\lambda}{D\cos\theta} + 4\varepsilon \tan\theta \quad (2)$$

$$\beta_{\text{total}}\cos\theta = 4\varepsilon \sin\theta + \frac{0.9\lambda}{D} \quad (3)$$

where ε is strain, λ is wavelength and D is crystallite size.

Given the fitted parameters breadth, β_{total} and peak position (2θ) for the Bragg peaks, a Williamson-Hall plot can be constructed to investigate the macrostrain and crystallite size of the material through a linear fit of breadth multiplied by cosine of the peak position against sine of the peak position and use of the values of gradient and intercept. The Williamson-Hall approach considers the breadth of a Bragg peak to be the result of both the size of the coherent domain in the direction of the scattering vector (assumed as a one-dimensional crystallite size) and strain. These are deconvoluted through plotting with respect to the peak position and finding the gradient and intercept of a linear fit (Eq. 3). We chose to apply the Williamson-Hall approach conjointly to the a- and c-related Bragg peaks within our dataset, in order to obtain mean microstrain and crystallite size values representative of the material as a whole, i.e. of all crystal orientations. We did investigate the applicability of applying the Williamson-Hall approach separately to the a- and c-related peaks. However, the minimal number of peaks in both cases then meant that the data were sparse and, hence, large scatter was present in the evaluated L_a and L_c values. These, in turn, led to large errors in the derived microstrain and crystallite size. In addition, due to the complexities of the origins of the (101) peak, we chose to exclude this from our Williamson-Hall plots.

Errors in fitting the Bragg peaks come from the inherent uncertainty in the measured intensity, which varies with the square root of the count. However, the main discrepancies in the results from Williamson-Hall plots are due to the linear fit to the data points derived from each peak, in this case four points. This can lead to some non-intuitive fits via minimising the square of the residual between the data, f_{data} , and the fit, f_{fit} .

2.3. Microstructure imaging

2.3.1. Focused ion beam

The microstructures of the graphites were examined using focused ion beam (FIB) milling. A dual-beam (FEI Helios Nanolab 600) was used to mill and image the sample material. Material was removed by sputtering to a depth of approximately 20 μm using a gallium beam of 30 keV energy and 21 nA current. The vertical face of the resulting trench was imaged (21 μm field-of-view, ~10 nm spatial resolution) using an electron beam. Image segmentation was performed using Vision Assistant (Labview), with manual adjustment.

2.3.2. X-ray tomography

A Zeiss Xradia 520 Versa x-ray tomography (XRT) microscope was used to obtain three-dimensional tomographic data from the graphite samples, with the x-ray source operating at 80 kV, 7 mA, and a 40x objective. This gave a 230 μm -wide field-of-view. ~700 nm voxel resolution image datasets were collected from three

regions within each specimen. Statistical analysis and quantification of the internal porosity were performed on the .tiff slices generated from each of the tomographic reconstructions. An adaptive image binarisation approach was used for image segmentation [22].

3. Results

3.1. Microstructure

As described in Section 2.1, the SNG graphites were prepared from petroleum coke and coal tar pitch. Hence, the overall microstructure comprised filler particles of typical 20 μm diameter embedded in a matrix of 'flour' particles and graphitised pitch. Depending on the specific fabrication history, there was between 8% and 18% porosity (Table 1).

Total porosities of SNG623 and SNG722 specimens, selected as representative of these graphites, were measured using series of FIB images to observe porosity at the nanometre to micrometre length-scale, in conjunction with x-ray tomography images to obtain porosity at the micrometre to millimetre length-scale. Fig. 3a and b compare typical fine-scale microstructures of sample material SNG623, as-captured by XRT and FIB serial sectioning. Fig. 3a shows a two-dimensional XRT image together with a representation of the three-dimensional reconstructed porosity at a voxel resolution of ~700 nm. By comparison, Fig. 3b presents a two-dimensional FIB cross-section imaged in the high-resolution secondary electron mode and corresponding porosity. This time-consuming exercise provided validation of the manufacturer's values for high- and low-porosity material (Table 1). This comparison emphasised that there was a combination of coarse and fine length-scale pores contributing to the total porosity for both the higher- and lower-porosity graphites.

3.2. X-ray diffraction

3.2.1. Temperature dependence of a and c lattice parameters

The variation of the XRD traces with temperature over the range from room temperature to 800 $^{\circ}\text{C}$ for the SNG342 axial and SNG722 axial graphite specimens are shown in Figs. 4–6. These were selected as they represent the extremes of porosity for the graphite samples (Table 1). There is a systematic change in the position of some diffraction peaks (2θ) with increasing temperature, and not others, i.e. (002) and (110) peaks, respectively. On returning back to room temperature, peaks reverted to their original 2θ diffraction positions. There is a complex overlap of diffraction peaks in the 2θ angular range 41 $^{\circ}$ to 47 $^{\circ}$, and these peaks, for the same graphite specimens, are shown in more detail in Fig. 6. These traces are typical of those observed previously for synthetic graphite (for example [13]). The diffraction patterns include a number of peaks attributable to the alumina sample holder, such as that located at ~43 $^{\circ}$ 2θ . As the surface of the sample holder is low with respect to the goniometer geometry - to accommodate the thickness of the graphite specimens - these alumina peaks are shifted relative to their literature values, with effects of temperature also recognisable in their 2θ position shifts.

From the positions of the diffraction peaks derived from the intensity maxima, and assuming that the graphite has a pseudo-hexagonal crystal structure, the variation in the lattice parameters a and c with temperature were established. Plots of these a and c values are presented in Fig. 7, where data derived from the (100) diffraction peak, and after taking into account instrument broadening, have been used to calculate the a values, and similar data from the (002) peak have been used to arrive at the plotted c values. With the c value, we observe a linear increase in value with increase in temperature ($\sim 2 \times 10^{-5} \text{ nm} \cdot \text{C}^{-1}$). By comparison, there

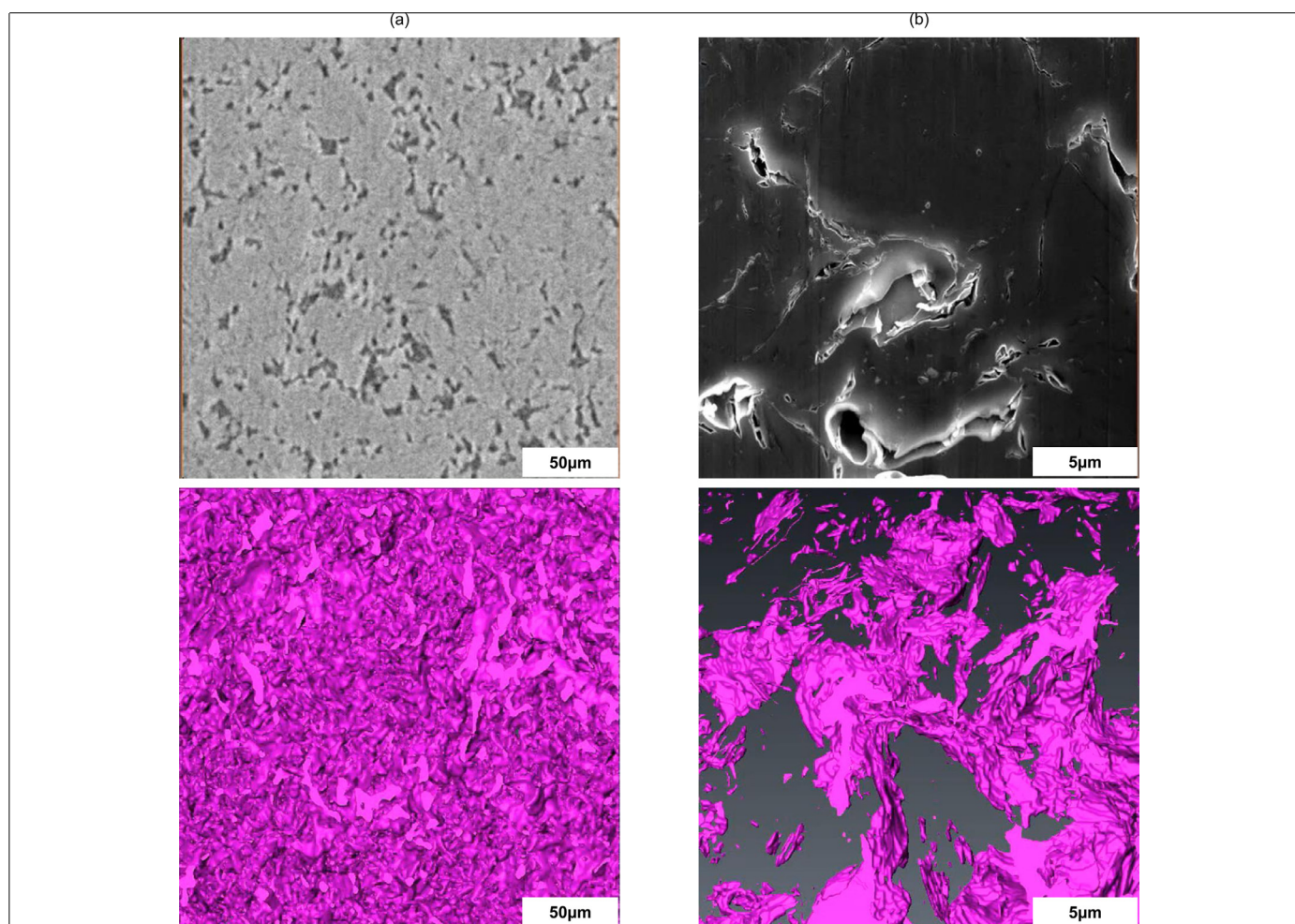


Fig. 3. Typical fine-scale microstructures of sample material SNG623, images and reconstructed porosities: a) x-ray tomography; b) focused ion beam.

is little variation of the a parameter over this temperature range. A similar trend was observed for all of the graphites examined in this work. In all cases, the diffraction traces, and therefore these two parameters, returned to the original room temperature values upon cooling. The observed temperature dependence trends are consistent with a literature summary of previous values of a and c reported by Morgan [7] for materials believed to be representative of nuclear grade graphites, though see Section 4.1 for a discussion on the mismatch in absolute values of c .

3.2.2. Coherence length/crystallite size

L_a and L_c , calculated using the Scherrer method (Eq. 1), and crystallite size, calculated using the Williamson-Hall approach (Eqs. 2 and (3)), versus temperature, and after consideration of instrumental broadening of the diffraction peaks, are given in Fig. 8. During heating from room temperature up to 800°C, L_a (the crystallite width, not to be confused with the a lattice parameter) is more sensitive to temperature than L_c (again, the crystallite thickness, and not the c axis lattice parameter), which remains stable.

Least square fits of microstrain versus temperature (Fig. 9), compiled from analyses of the graphite samples during heating from room temperature to 800°C, are close to zero slope. Hence, the microstrains are small and there is no measurable change with temperature. Also, comparison of microstrain versus temperature before and after taking into account the instrumental broadening confirms, in agreement with the literature, that the existence

of strain is one factor which can induce peak broadening (Eq. 2) [10,23,24].

4. Discussion

Graphite is recognised to have a complex microstructure, even in its simplest form, and this becomes more complicated with synthetic, polygranular graphites of the type considered in this paper. The complexity arises from several sources, but with a simple graphite it is associated with the fact that it comprises graphene sheets stacked one above the other so that any variations in the sequence can lead to differences in the overall crystal structure. Bernal [25] established by XRD the simplest hexagonal layer arrangement of carbon atoms to be in an ABAB... sequence. The presence of rhombohedral structures was further confirmed by Bacon [26]. In addition, turbostratic graphite has been reported where carbon layers are aligned, but randomly rotated with respect to each other. This apparent disorder leads to some of the problems encountered in correlating measured physical and mechanical properties with specific variants of synthetic, polygranular graphite. For the coke filler and binder carbon matrix in an isostatically-moulded graphite of the type considered in this present work, März et al [16] proposed a turbostratic-like laminate arrangement where graphite crystallites are oriented parallel to the basal plane but rotated randomly.

The variation of lattice parameters a and c with temperature for the synthetic polygranular graphites considered in Fig. 7 are

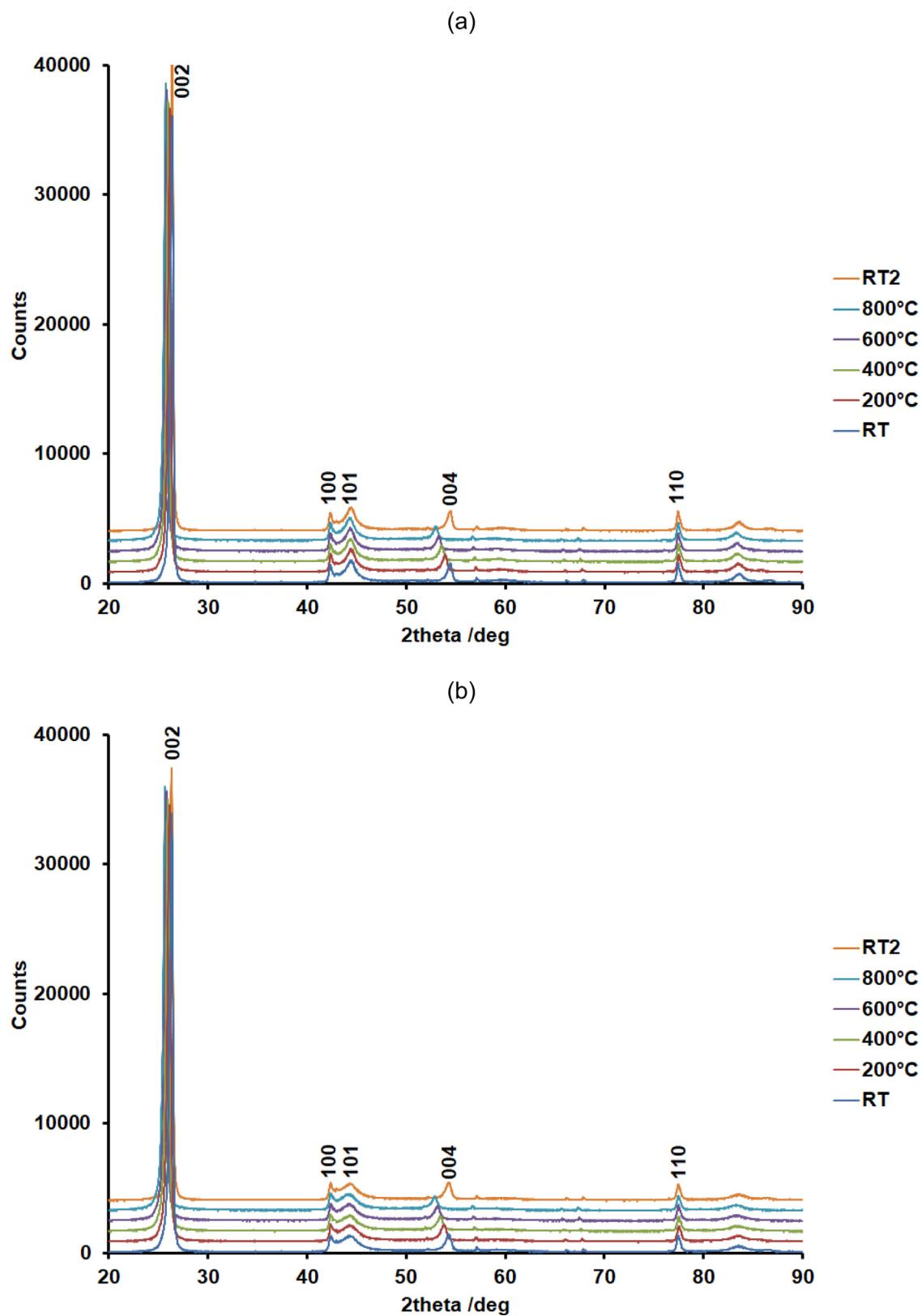


Fig. 4. Variation with temperature of x-ray diffraction traces for representative SNG graphites: a) SNG342 axial; b) SNG722 axial.

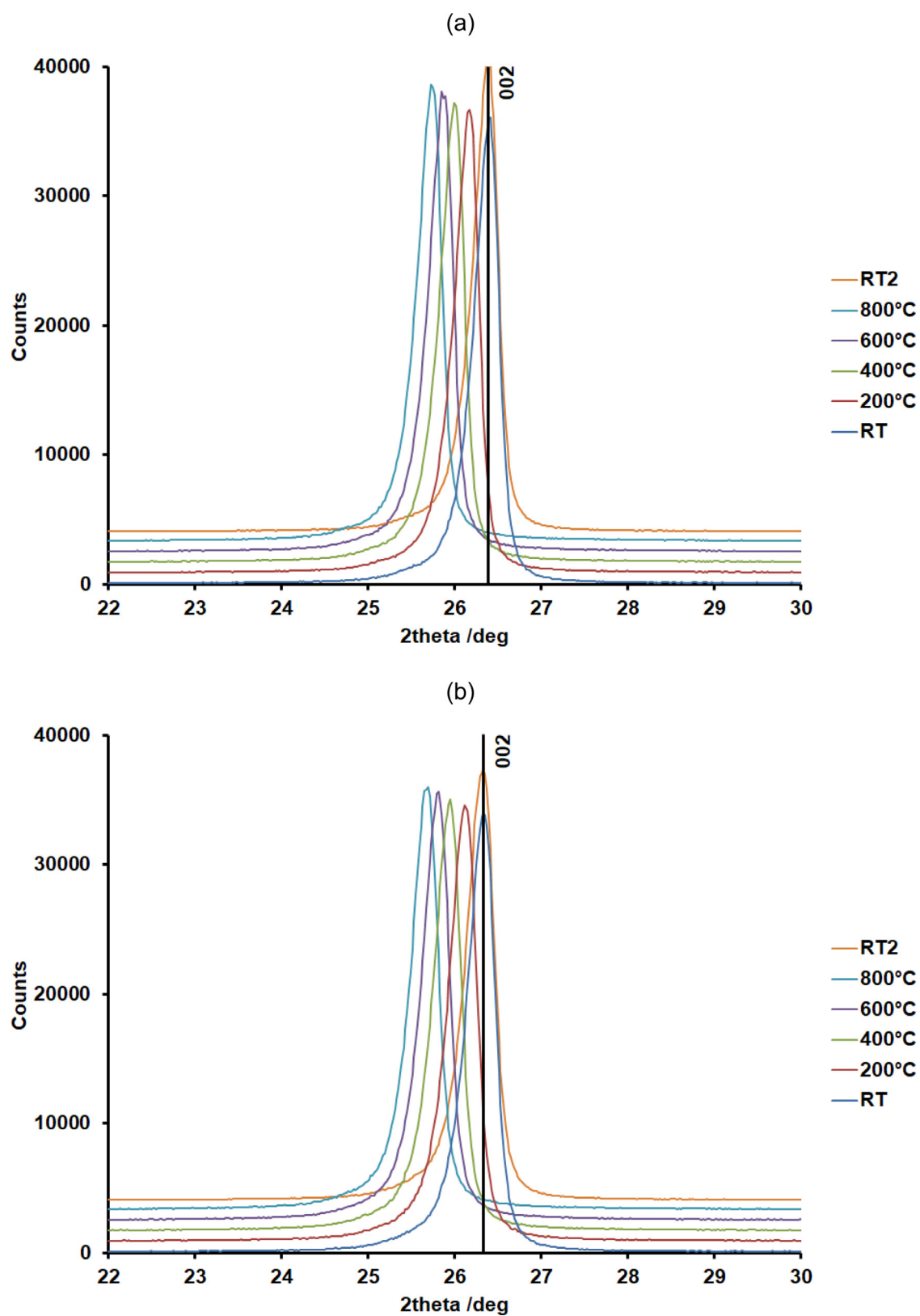


Fig. 5. Variation with temperature of x-ray diffraction traces for representative SNG graphites, in the 22° to 30° region: a) SNG342 axial; b) SNG722 axial.

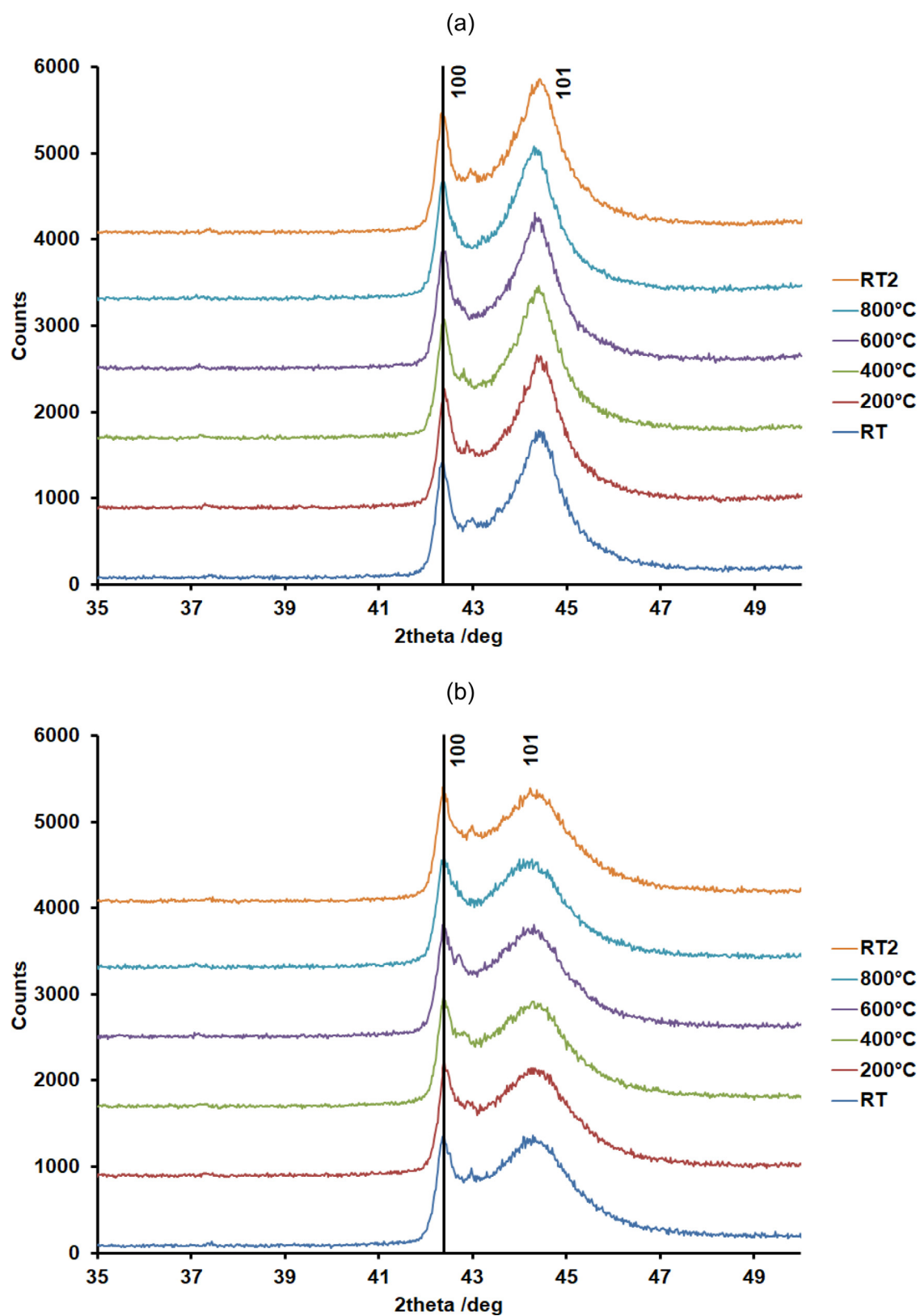


Fig. 6. Variation with temperature of x-ray diffraction traces for representative SNG graphites, in the 35° to 50° region: a) SNG342 axial; b) SNG722 axial.

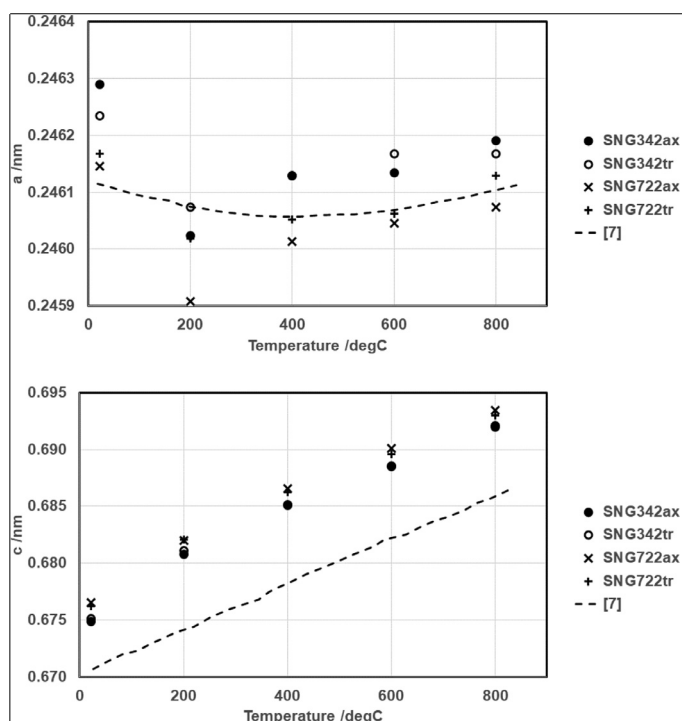


Fig. 7. a and c values versus temperature derived from (100) and (002) peak data, respectively, for representative SNG graphites: SNG342 axial and transverse; SNG722 axial and transverse - compared to data from [7].

consistent with values described by Morgan [7]. In general, there is a small increase in the value of a , by $\sim 0.0001\text{nm}$ ($\sim 0.04\%$), for the higher-porosity graphite (18%) compared to the lower-porosity material (8%). Although the scale of this change is within the resolution of our tests, the effect this has and its significance for the material as a whole requires further investigation and will be the subject of future synchrotron experiments. There is also a corresponding, but more significant, decrease in the c lattice parameter of $\sim 0.002\text{nm}$ ($\sim 0.3\%$). Over the room temperature to 800°C range, it is the c lattice parameter that increases monotonically with temperature (Fig. 7). It is important to recognise that both lattice parameters returned to their original values when cooled from 800°C to room temperature. These changes with temperature in the a and c lattice parameters are consistent with the strong sp^2 -hybridised bonds between carbon atoms within the basal planes and the weak van der Waals bonds between basal planes.

It is noteworthy that, for many decades, there has been a recognition of the complexity of the perfection of the local arrangements of atoms within naturally-occurring and synthetic graphites. Historically, graphites have been classified by a measure of crystal perfection. This has been characterised by a parameter, p , which is defined to provide a measure of the proportion of misoriented carbon atom layers; perfect graphite has $p=0$ while, for example, highly-disordered coke prepared via low-temperature carbonisation has $p \approx 1$ [27]. From the c lattice parameter values at room temperature (e.g. Fig. 7), our SNG graphite materials have interlayer spacings, d , of between 0.3374nm and 0.3381nm . By comparison with the experimental curve of Bacon [26], such interlayer spacings represent p parameter values of approximately 0.5 to 0.6. Fig. 10 re-presents c lattice parameter values, converted to interlayer spacings, d , against temperature for the representative SNG graphites (SNG342 axial and transverse; SNG722 axial and transverse), and compares these to the trends with different values for the perfection parameter, p , taken from Kellett, Jackets and Richards [28]. The data from measurements in this work are con-

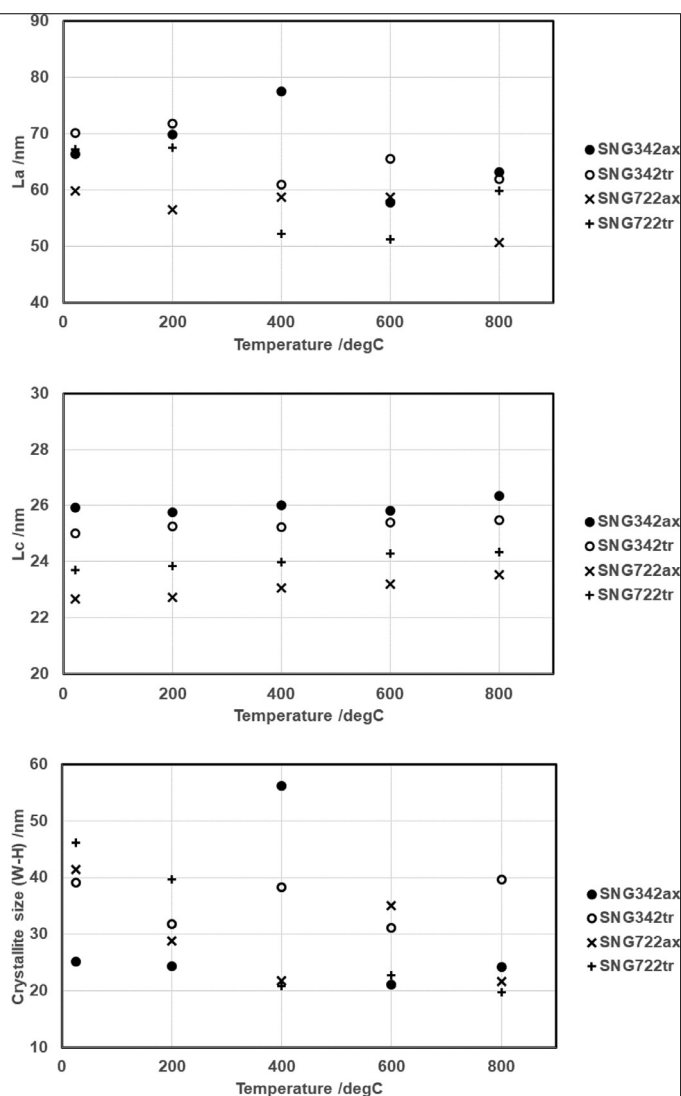


Fig. 8. L_a , L_c and Williamson-Hall crystallite size values versus temperature for representative SNG graphites: SNG342 axial and transverse; SNG722 axial and transverse.

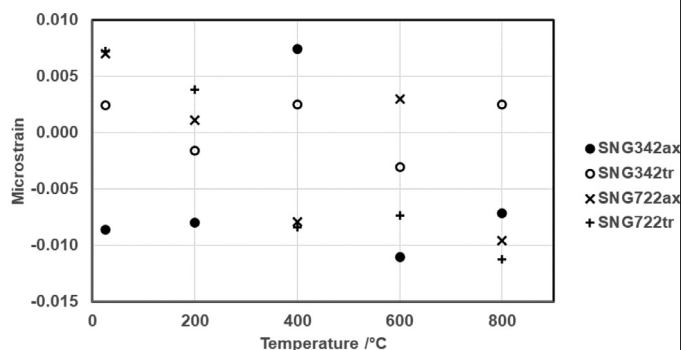


Fig. 9. Microstrain versus temperature for representative SNG graphites: SNG342 axial and transverse; SNG722 axial and transverse.

sistent with p values for the SNG graphites of the order of 0.6. The difference for the measured lattice parameters, when compared to literature data (Fig. 7), clearly indicates that the graphites described by Morgan [7] have far lower p values, i.e. contain significantly less disorder than the SNG nuclear reactor graphites analysed here.

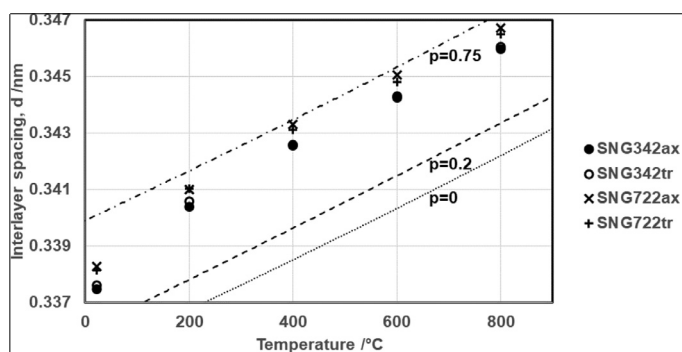


Fig. 10. Interlayer spacing, d , versus temperature for representative SNG graphites: SNG342 axial and transverse; SNG722 axial and transverse - compared to trends with differing perfection parameter, p . Adapted from Kellett, Jackets and Richards [28].

XRD peak widths provide a measure of coherence length in the direction of the diffraction vector. This parameter is one that can be linked to crystallite size averaged over the filler and binder matrix for the present SNG graphites. As pointed out in the Introduction, XRD samples over a relatively large volume of material compared with some other techniques, thereby providing average values for L_a and L_c over dimensions representative of this complex microstructure. Consequently, we consider it not to be instructive, in the context of this present paper, to make direct comparisons with TEM without having a significant number of specimens for the latter to make the comparison appropriate. Hence, measures of these length-scales with temperature derived from analysis of the x-ray peaks for L_a and L_c using the Scherrer procedure (Eq. 1) are compared with average dimensions obtained from the Williamson-Hall analyses (Eqs. 2 and (3) (Fig. 8). The latter approach allows discrimination of coherence length and microstrain despite both contributing to the profile of the XRD peaks. For the present material, there is overlap within the range of the (100) and (101) diffraction peaks. Although peak-fitting procedures have been adopted to deconvolute these two diffraction peaks, the (101) shows unusually large broadening, which has been observed in some graphites by other workers [16]. The overlap and excessive broadening of the (101) peak for the present graphite is potentially a result of the specific production route adopted and could arise from several factors, including multiple phases, turbostratic strain and defect structure [29,30]. In general, the layered nature of the graphite allows the (101) crystallographic plane interspacing to accommodate such features and defects. The data collected in this work show no other peaks which can be indexed as part of a separate graphite phase. This suggests that the intensity observed in the (100) to (101) range is an effect of complex defect structures not contained in a particular crystallographic plane.

In an attempt to quantify the simpler inhomogeneous strain, the asymmetry of individual peaks was considered. In all samples, at all temperature, the (001) direction shows inhomogeneous expansion and the (100) shows compression. In Fig. 8 we observe a small overall downward change in the Scherrer-derived L_a with temperature, while the change in L_c is negligible in comparison, though still presenting a slight increase with temperature. The mean Williamson-Hall crystallite size value exhibits a small decrease, consistent with the previously-observed change in L_a . It should be noted that the Williamson-Hall approach, as we have implemented it, provides a measurement that represents an average of the different crystallographic orientations and, because of that, the microstrain is evaluated. The microstrain as a function of temperature (Fig. 9) is small, ranging between approximately -0.008 and 0.008 . The errors in these strain measurements are $\sim 5 \times 10^{-5}$, which comes from the error in the Williamson-Hall fit.

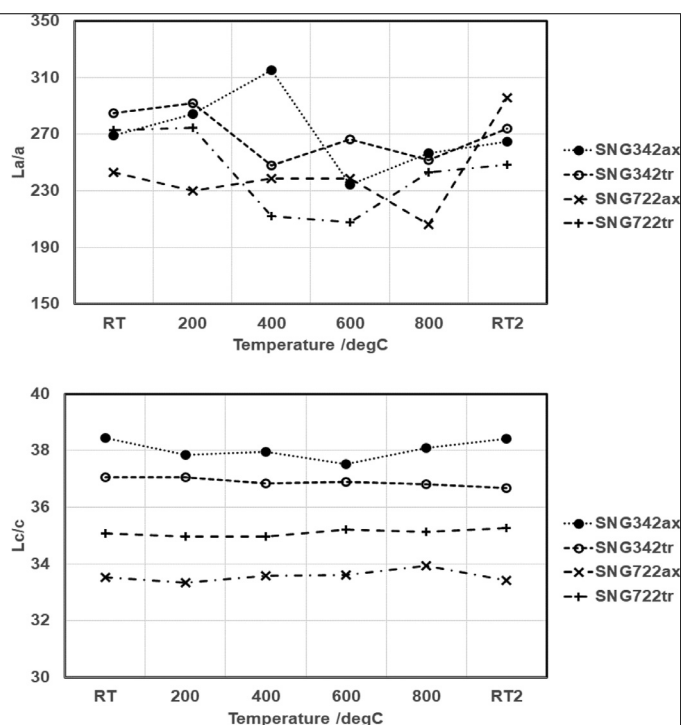


Fig. 11. L_a/a and L_c/c versus temperature for representative SNG graphites: SNG342 axial and transverse; SNG722 axial and transverse. n.b. Room temperature (22°C) values at start and finish of temperature cycle.

There is some variability around zero, but otherwise no temperature dependence.

Although there is an increase in spacing between the basal plane layers, c , with temperature and a small variation in a , as shown in Fig. 7, there is no change in peak broadening to illustrate a systematic change in coherence length (Fig. 8). The data in Fig. 8 reveal a small, $\sim 2\text{nm}$, difference in L_c between the higher-porosity (18%) graphite and that with $\sim 8\%$ porosity. The standard interpretation is to equate coherence length with crystallite size, as discussed in the Introduction. This parameter would then show if there is any significant change in the numbers of atoms making up crystallite volumes at these temperatures. Fig. 11 presents the results in terms of absolute numbers of lattice planes, obtained by dividing L_a and L_c by the respective lattice parameters. As the change in a with temperature is small, in absolute terms, the plot of L_a/a closely mirrors that of L_a (Fig. 8). Therefore, there is a small overall downward change in L_a/a with increase in temperature, which is then reversed when reverting the specimens back to room temperature. With L_c/c , the increase in c with temperature acts to counter the previously-seen minimal increase in L_c , resulting in little discernible change through the temperature range, from room temperature up to 800°C and back to room temperature. Therefore, in the c direction graphite crystallite expansion with increase in temperature is due to the equivalent expansion of the interlayer spacing. On the other hand, in the a direction our results indicate the formation of (reversible) lattice defects with temperature, that act to reduce the coherence length (crystallite size), while the lattice parameter is little-affected.

Crystallite formation and growth in graphitised carbon has been considered by Franklin [31] to arise from carburisation of hydrocarbon components (between 220°C and 450°C , depending on the hydrocarbon), in this case within the original materials used for manufacture of the synthetic graphite. However, in the present case the specimens have already seen a significant thermal history at high temperatures to graphitise the material. However, during XRD analysis there was expansion of the graphite lattice spacing

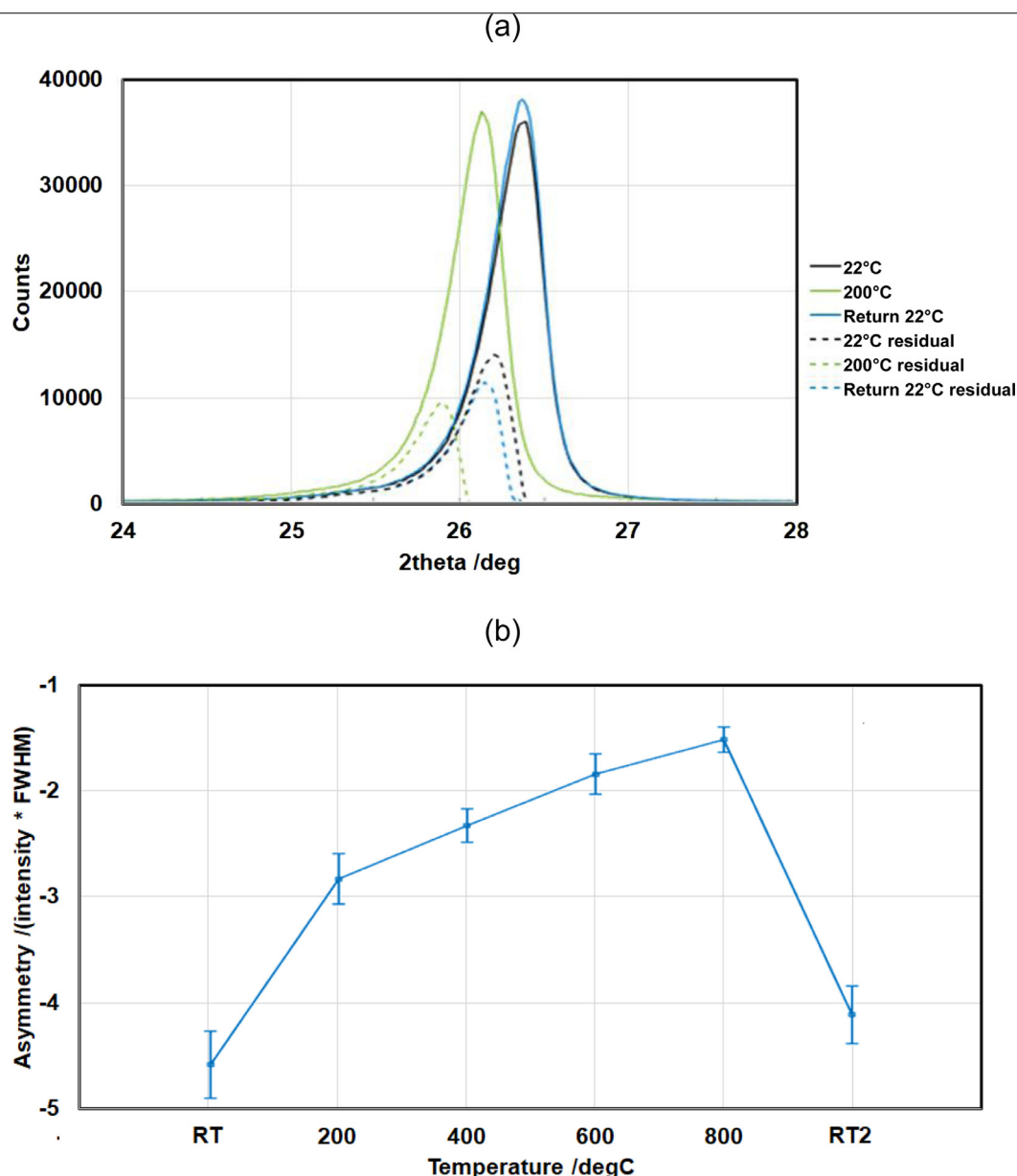


Fig. 12. a) SNG3420ax (002) XRD traces (RT, 200°C and after return to RT; solid lines), and residual asymmetric intensity, relating to the inhomogeneously-strained volume (dashed lines). b) Mean (002) peak asymmetry across all specimens normalised by weight of the fitted peak; error bars show 1σ standard deviation from mean; negative values denote asymmetry at lower angle than main peak.

in the weakly-bonded c direction as the temperature was increased to 800°C. As highlighted earlier in this work, the presence of defects in these materials would cause the asymmetry in XRD peaks which is indicative of inhomogeneous strain. There is a range of proposed defect structures within graphite, and interrogation of individual peaks cannot isolate which are responsible for the effect observed [29]. The shift in peak location (a and c change) is accompanied by a reduction in the amount of asymmetry observed as the temperature increases. This suggests that the volume responsible for the asymmetry reacts differently with temperature than the un-strained graphite material. Interestingly, asymmetry (see Section 2.2.2) decreases after the temperature cycle (Fig. 12). With no corresponding change in microstrain (Fig. 9), the temperature increase and lattice change possibly illustrate a decrease in the contribution from defects. Other studies, using Raman spectroscopy, have seen removal of neutron and ion radiation defects from graphite through annealing over this temperature range [32].

The specimens were prepared by mechanical grinding and consideration should be given to its possible effect. The damaged surface layers arising from machining has been measured by el Turke² using taper-section specimens of SNG and HOPG graphites. These measurements indicate that the damaged layer for the former was ~12µm thick and for the latter ~6µm thick. In this XRD study, the detection and position of the alumina diffraction peaks arising from the holder provided indications that these graphite specimens were sampled through-section. The alumina peak positions were displaced from their reference 2θ values due to the displacement of the analysed holder plane by the thickness of the specimens, i.e. approximately 800µm to 900µm. Hence, the incident x-ray beam was sampling up to ~900µm thickness, leading to the possible deformed layer representing only a very small contribu-

² A el-Turke, private communication (2021).

tion of the total diffraction signal. It is worth mentioning that if the asymmetry in the peak was due to the height discrepancy of the signal arising from material between the sample top and bottom then the asymmetry would not be lost on heating (it might possibly increase with expansion). This leaves the source of the inhomogeneous strain as an open question.

Neutron and Raman scattering studies have shown that similar polygranular nuclear graphites contain significant elastic strains, due to their production route and the anisotropy of thermal expansion and elastic moduli, and that these strains can be affected by mechanical loading [33]. We observe in this work that cycling to a moderate temperature causes lattice size changes that are fully-reversible, with no permanent change in crystallite size or microstrain. However, the amount of inhomogeneous strain is decreased. It is possible that the lattice expansion with temperature allows for more defect mobility, thereby allowing relaxation of the local inhomogeneous strains. Further information is required to understand this phenomenon fully. This aspect, together with the true nature of the defects that lead to the complex (100) to (101) peak overlap, requires higher-resolution and lower-background data to allow for quantitative assessment of defect densities that may be obtained through x-ray synchrotron diffraction experiments.

5. Conclusions

The synthetic, polygranular graphites considered in this paper have complex microstructures. Higher porosity in the graphite was accompanied by higher *a* and *c* lattice parameters compared to lower porosity material. The *c* lattice parameter increases monotonically with temperature ($\sim 2 \times 10^{-5} \text{ nm.C}^{-1}$). Both *a* and *c* lattice parameters return to original values when cooled back to room temperature.

The interlayer spacings, *d*, of between 0.3374 nm and 0.3381 nm represent *p* parameter values of ~ 0.5 to ~ 0.6 in these particular graphite materials.

The overlap and excessive broadening of the (101) peak for these graphites is potentially a result of the production route, arising from factors such as multiple phases, turbostratic strain and defect structure. The (101) plane interspacing can accommodate such features and defects.

There is a small difference in *L_c* between the high- and low-porosity graphites, though *L_a*, *L_c* and mean Williamson-Hall crystallite size are invariant with temperature over the range considered. Thermal cycling had no effect on measured crystallite size.

Microstrain is small, ranging between approximately -0.008 and 0.008 as a function of temperature.

There is no systematic change in coherence length (crystallite size) with temperature.

Graphite expansion with increase in temperature in the weakly-bonded *c* direction is accommodated for by an equivalent expansion of the interlayer spacing, whereas in the *a* direction we see indications of the formation of (reversible) lattice defects with temperature, that act to reduce the coherence length (crystallite size), while the lattice parameter is little affected. The lattice changes are fully-reversible when the graphite is returned to room temperature, but some inhomogeneous strain is removed.

Data Access Statement

Data are available from the University of Bristol data repository, data.bris, at <https://doi.org/10.5523/bris.14xzwi4gmzqkd26a2qblw9m8o6>.

Declaration of Competing Interest

The authors declare that they have no known competing financial interests or personal relationships that could have appeared to influence the work reported in this paper.

Acknowledgments

The authors thank EPSRC for providing funding for this programme of work (grant references EP/M018598/1 and EP/M018679/1) and Professor Houzheng Wu (Loughborough University) for provision of material and helpful discussions. PEJF thanks Wolfson College, Oxford for facilitating the collaboration.

References

- [1] PJ Heard, L Payne, MR Wootton, PEJ Flewitt, Evaluation of surface deposits on the channel wall of trepanned reactor core graphite samples, *J. Nucl. Mater.* 445 (2014) 91–97.
- [2] BE Mironov, AVK Westwood, AJ Scott, R Brydson, AN Jones, Structure of different grades of nuclear graphite, *J. Phys. Conf. Ser.* 371 (2012) 012017.
- [3] N Nemeth, RL Bratton, Overview of statistical models of fracture for nonirradiated nuclear-graphite components, *Nucl. Eng. Des.* 240 (2010) 1–29.
- [4] B Marsden, A Mummery, P Mummery, Modelling the coefficient of thermal expansion in graphite crystals: implications of lattice strain due to irradiation and pressure, *Proc. R. Soc. A* 474 (2018) 20180075.
- [5] BJ Marsden, M Haverty, W Bodel, GN Hall, AN Jones, PM Mummery, et al., Dimensional change, irradiation creep and thermal/mechanical property changes in nuclear graphite, *Int. Mater. Rev.* 61 (2016) 155–182.
- [6] DP Riley, Thermal expansion of graphite: part II theoretical, *Proc. Phys. Soc.* 57 (1945) 486–495.
- [7] WC Morgan, Thermal expansion coefficients of graphite crystals, *Carbon* 10 (1972) 73–79.
- [8] PJ Hacker, GB Neighbour, B McEnaney, The coefficient of thermal expansion of nuclear graphite with increasing thermal oxidation, *J. Phys. D Appl. Phys.* 33 (2000) 991–998.
- [9] H Badenhorst, Microstructure of natural graphite flakes revealed by oxidation: Limitations of XRD and Raman techniques for crystallinity estimates, *Carbon* 66 (2014) 674–690.
- [10] L Alexander, HP Klug, Determination of crystallite size with the x-ray spectrometer, *J. Appl. Phys.* 21 (1950) 137–142.
- [11] R Krishna, J Wade, AN Jones, M Lasithiotakis, PM Mummery, BJ Marsden, An understanding of lattice strain, defects and disorder in nuclear graphite, *Carbon* 124 (2017) 314–333.
- [12] GK Williamson, WH Hall, X-ray broadening from filed aluminium and wolfram, *Acta Metall.* 1 (1953) 22–31.
- [13] VS Babu, MS Seehra, Rietveld profile refinement of the x-ray diffraction patterns of graphite, in: 21st Biennial Conference on Carbon, June, 1993, pp. 665–666.
- [14] ZQ Li, CJ Lu, ZP Xia, Y Zhou, Z Luo, X-ray diffraction patterns of graphite and turbostratic carbon, *Carbon* 45 (2007) 1686–1695.
- [15] C Karthik, J Kane, DP Butt, WE Windes, R Ubi, Microstructural characterization of next generation nuclear graphites, *Microsc. Microanal.* 18 (2012) 272–278.
- [16] B März, K Jolley, TJ Marrow, Z Zhou, M Heggie, R Smith, et al., Mesoscopic structure features in synthetic graphite, *Mater. Des.* 142 (2018) 268–278.
- [17] Z Zhou, WG Bouwman, H Schut, C Pappas, Interpretation of x-ray diffraction patterns of (nuclear) graphite, *Carbon* 69 (2014) 17–24.
- [18] P Klug, Alexander LE, X-ray diffraction procedures: For polycrystalline and amorphous materials, Wiley, New York, 1974.
- [19] AR Stokes, AJC Wilson, The diffraction of x-rays by distorted crystal aggregates - I, *Proc. Phys. Soc.* 56 (1944) 174–181.
- [20] BE Warren, X-ray diffraction in random layer lattices, *Phys. Rev.* 59 (1941) 693–698.
- [21] M Zinkin, Recursive minimisation program, Institut Laue-Langevin, 14 June 1996 Revised: E Farhi, D McMorrow, 03 January (2000).
- [22] J Sauvola, M Pietikäinen, Adaptive document image binarization, *Pattern Recognit.* 33 (2000) 225–236.
- [23] S Sivasankaran, K Sivaprasad, R Narayanasamy, PV Satyanarayana, X-ray peak broadening analysis of AA 6061_{100-x} - x wt.% Al₂O₃ nanocomposite prepared by mechanical alloying, *Mater. Charact.* 62 (2011) 661–672.
- [24] MA Senthil Saravanan, K Sivaprasad, P Susila, SP Kumaresh Babu, Anisotropy model in precise crystallite size determination of mechanically alloyed powders, *Physica B* 406 (2011) 165–168.
- [25] JD Bernal, The structure of graphite, *Proc. R. Soc. A* 106 (1924) 749–773.
- [26] GE Bacon, The interlayer spacing of graphite, *Acta Crystallogr.* 4 (1951) 558–561.
- [27] EA Kellett, BP Richards, The thermal expansion of graphite within the layer planes, *J. Nucl. Mater.* 12 (1964) 184–192.
- [28] EA Kellett, BP Richards, A study of the amplitude of vibration of carbon atoms in the graphite structure, *Carbon* 2 (1964) 175–183.

- [29] MI Heggie, I Suarez-Martinez, C Davidson, G Haffenden, Buckle, ruck and tuck: a proposed new model for the response of graphite to neutron irradiation, *J. Nucl. Mater.* 413 (2011) 150–155.
- [30] H Wub, R Gakhar, A Chen, S Lam, CP Marshall, RO Scarlet, Comparative analysis of microstructure and reactive sites for nuclear graphite IG-110 and graphite matrix A3, *J. Nucl. Mater.* 528 (2020) 151802.
- [31] RE Franklin, Crystallite growth in graphitizing and non-graphitizing carbons, *Proc. R. Soc. A* 209 (1951) 196–218.
- [32] M Lasithiotakis, BJ Marsden, TJ Marrow, Annealing of ion irradiation damage in nuclear graphite, *J. Nucl. Mater.* 434 (2013) 334–346.
- [33] TJ Marrow, D Liu, SM Barhli, L Saucedo Mora, Ye Vertyagina, DM Collins, et al., In situ measurement of the strains within a mechanically loaded polygranular graphite, *Carbon* 96 (2016) 285–302.